



Cite this: *Phys. Chem. Chem. Phys.*,
2024, 26, 14866

Layer-dependent spin texture and origins of Rashba splitting quenching in the 2D CsPbI_3 perovskite

Safieh Nazari *^a and Yavar T. Azar  ^b

The spin-orbit coupling in inorganic perovskite materials containing heavy elements causes interesting electronic characteristics such as Rashba and Dresselhaus effects. Several studies have reported significant band splitting in the presence of asymmetry, while the impacts of the external field strength, surface termination on the electronic structure still need to be resolved. In the current study, a systematic relation between the external parameters and the band splitting in CsPbI_3 slabs is clarified through first-principles calculations. Here, we examine the band splitting and spin patterns of CsPbI_3 slabs exposed to an external electric field ranging from zero to hundreds of kV cm^{-1} . Our results indicate apparent non-linear behavior of the Rashba coefficient along with a turning point for the band splitting for a definite external field. Here, the origin of this quench in the band splitting is explained in terms of spatial localization of the wave functions and clear change in their center of charge going from low to high electric fields. The findings not only explain the origin of quenching band splitting but also reveal the external field's significance in the spin texture and recombination rate of 2D perovskites. The current research outcome paves the way for atomic scale engineering of perovskite materials for a wide range of applications.

Received 14th January 2024,
Accepted 19th April 2024

DOI: 10.1039/d4cp00165f

rsc.li/pccp

1 Introduction

The last decade has witnessed a rapid surge of interest in developing hybrid organic/inorganic perovskites (HOPs). Tremendous research efforts on the compositional design and mechanisms behind the efficient operation of these materials has extended their application in photovoltaics, optoelectronics, field-effect transistors, memristors, and more.^{1–4} After the astonishing leap in efficiency of perovskite-based photovoltaic devices, numerous suggestions have been made for their application in other fields. In particular, having heavy elements with effective spin-orbit coupling (SOC) makes them potential candidates for spintronics applications.⁵ Theoretical and experimental research has been conducted over the last few years and has revealed the Rashba-type⁶ band splitting in hybrid organic/inorganic halide perovskites through symmetry breaking.⁷ The giant spin-orbit coupling (SOC) in this family is accepted as the main origin of Rashba-like splittings in their band structures.^{8,9}

From a theoretical point of view, structural asymmetry plays a central role in the appearance of spin-polarization. This asymmetry can be rooted in the external field, interfacial

built-in field, and geometrical distortion.¹⁰ Shanavas *et al.* showed that perovskite structures in the presence of an applied electric field are ideal systems for tunable Rashba splitting.¹¹ In addition, Myung *et al.* declared that the inversion symmetry breaking field at the interfaces between perovskite and substrate, exhibits remarkable band splitting.¹² Chen *et al.* studied the influence of an external electric field on bilayer CsPbBr_3 , indicating a significant different between the Rashba coefficient attributed to different terminations.¹³ A similar Rashba effect has been observed for other 2D perovskites in the presence of an electric field. 2D orthorhombic RbSnI_3 as a prominent example, exhibits the largest Rashba parameter among all members of this family.¹⁴

Despite all the above-mentioned efforts on the characterization of spin-polarization as a function of external variables, the characteristic SOC-induced band splitting in 2D CsPbI_3 has yet to be dealt with in depth. In this context, the current study employing an *ab initio* approach calls into question the geometry- and field-induced modifications in the band structure and the spin texture of 2D films. Our results demonstrate the complicated behavior of the band splitting and the spin texture through changes in the external electric field. Deepening our understanding of what is happening in these systems could be the cornerstone for the purposeful design of these materials for various applications.

^a Physics and Accelerators Research School, Nuclear Science and Technology Research Institute, Tehran, Iran. E-mail: nazari.s@gmail.com
^b Physics and Accelerators Research School, AEOI, Tehran, Iran

2 Computational materials

All calculations were carried out using the quantum-ESPRESSO^{15,16} DFT package with the Perdew–Burke–Ernzerhof (PBE) version of the generalized gradient approximation (GGA).¹⁷ The electronic wave functions are expanded onto a plane-wave basis set with the kinetic energy cut-off of 35 Ry. Fully relativistic pseudopotentials are used for Pb 5d6s6p, I 5s5p, and Cs 6s.

The CsI-terminated and PbI_2 -terminated slabs are considered in (001), as a function of thickness n , which denotes the number of octahedrals, and about 18 Å vacuum between consecutive images to model perovskite surfaces. The $6 \times 6 \times 1$ Monkhorst–Pack grids are used for Brillouin-zone (BZ) sampling for the optimization and self-consistent field (SCF) calculations. The atomic positions are relaxed until the residual forces on each atom become less than 0.001 Ry Bohr⁻¹.

Utilizing the various implementations of DFT can create small changes in the simulation results. While Quantum espresso benefits from the accuracy of the plane-wave basis set, the methods based on the linear combination of atomic orbitals (LCAO) have significant savings in the cost of calculations. In this work, the recent development of the SOC in Siesta package^{18–20} has been employed to examine the sensitivity of band-splitting and spin-texture results to the level of theory.

3 Results and discussion

3.1 Interplay of the external field and SOC-induced band splitting

In the presence of a spin-orbit coupling system the Hamiltonian at the first approximation can be written as

$$\mathcal{H} = \sum_{i=1}^N \frac{\left(\mathbf{p}_i + \frac{e\mathbf{A}(\mathbf{r}_i)}{c}\right)^2}{2m} + \sum_{i=1}^N V(\mathbf{r}_i) + \mathcal{H}_{\text{SO}} \quad (1)$$

where $V(\mathbf{r}_i)$, \mathbf{p}_i and $\mathbf{A}(\mathbf{r}_i)$ stand for the electrostatic potential, the momentum operator and vector potential, respectively. The last term in the above equation is denoted as \mathcal{H}_{SO} which adds the SOC contribution to the unperturbed Hamiltonian \mathcal{H} ,

$$\mathcal{H}_{\text{SO}} = \frac{\hbar}{4m^2c^2} \sum_{i=1}^N (\nabla V(\mathbf{r}_i) \times \mathbf{p}_i) \cdot \boldsymbol{\sigma} \quad (2)$$

where $\boldsymbol{\sigma}$ is the Pauli matrices vector. The above Hamiltonian can be rewritten considering $\mathbf{k} \cdot \mathbf{p}$ theory and symmetries in the system. The α -CsPbI₃ phase of the perovskite has the $Pm\bar{3}m$ (no. 221) space group with five atoms in the primitive unit cell. Cs, Pb and I atoms set up in Wyckoff positions, a, b, c and $m\bar{3}m$, $m\bar{3}m$ and $4/mmm$ site symmetries, respectively. Truncation of the bulk structure perpendicular to the c -axis with two possible CsI- and PbI_2 terminations yields two 2D slabs with $P4mm$ (no. 99) space group. For this slab model with high symmetry C_{4v} point group, above perturbation reduces to the so-called

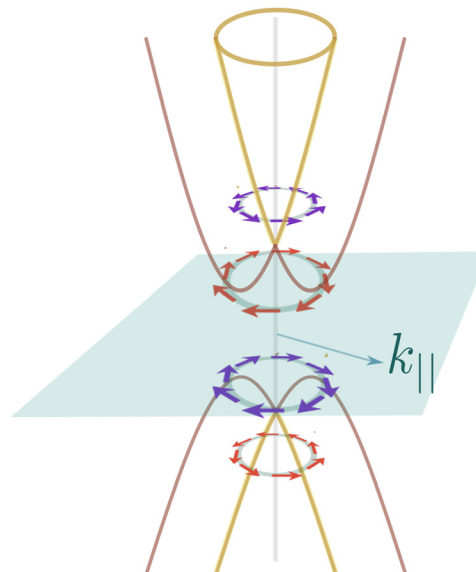


Fig. 1 Inner and outer branches of the band are depicted in brown and gold after Rashba-splitting, circular arrows show the spin texture for each branch.

Rashba Hamiltonian:²¹

$$\mathcal{H}_{\text{R}} = \alpha_{\text{R}} (k_x \sigma_y - k_y \sigma_x). \quad (3)$$

The Rashba parameter (α_{R}) can be calculated from band splitting at the close vicinity of the special k -point

$$\alpha_{\text{R}} = \frac{\Delta E}{2k_{\parallel}} \quad (4)$$

where k_{\parallel} is the \mathbf{k} vector in the $k_x k_y$ plane. Lifting the spin degeneracy by means of the ideal Rashba splitting is visualized in Fig. 1.

In this work, we investigate the electronic structure of two different CsPbI₃ terminations in the presence of the external electric field. Applying the external field significantly affects the electronic structure of the systems, in particular SOC-induced band splittings. In this regard, in the remainder of this article the effect of the external electric field on the charge distribution, the band splitting, and the spin pattern are explored for two different terminations.

3.2 Charge polarization in the external field

Charge redistribution and potential variation are the two most intuitive changes that can be observed in systems after applying an external field, and have a significant impact on the electronic structure. Therefore, the first part of our results address the slab's polarization in detail. The charge and potential for both slabs are calculated before and after applying the external electric field and are illustrated in Fig. 2, for thickness $n = 3$. As can be seen, there is a clear charge transfer along with electric potential gradient. More in depth exploration of the charge difference pattern indicates stronger polarization effects at the space near the atomic centers.

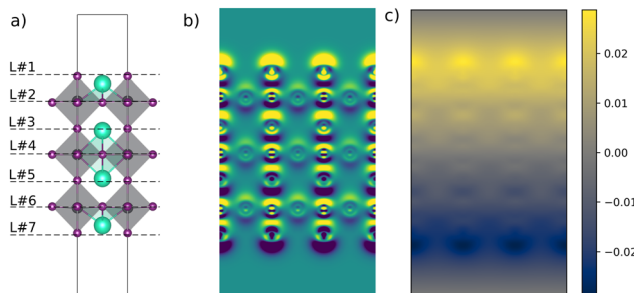


Fig. 2 The structure of a CsI-terminated slab with atomic layers labeled from the top to bottom (a), and 2-dimensional representation of the field-induced charge displacement along the Y - Z plane, yellowish and darkish green regions represent charge accumulation and depletion regions, respectively (b). 2D-Representation of the field induced changes in the electrostatic potential along the Y - Z plane (c).

While one can expect unequal changes for different atomic layers in the z -direction, regarding the periodic geometry of these slabs in the xy -plane there is no significant redistribution over the xy -plane. Hence, the planar averaged charge can be calculated as follows:

$$\bar{\rho}(z) = \int \rho(\mathbf{r}) dx dy. \quad (5)$$

In a same way one can calculate the planar average for the electrostatic potential before and after the external field application to gain more insight into the system response. For instance, considering thickness $n = 3$, the averaged induced charge, $\Delta\bar{\rho}(z) = \bar{\rho}_E(z) - \bar{\rho}_{E=0}(z)$, is calculated and depicted in Fig. 3 for both CsI- and PbI_2 terminated slabs. The successive peaks in the $\rho(z)$ plots are attributable to the consecutive atomic layers, $\dots/\text{PbI}_2/\text{CsI}/\text{PbI}_2/\dots$, and valleys between these peaks are indicative of interstitial space between the atomic layers. As seen in both cases, surface layers are more polarized compared to the interior atomic layers. Also, comparing the polarization of individual atomic layers in each case demonstrates a higher polarization of the PbI_2 layers compared with the CsI ones.

3.3 The electronic structure

Due to heavy elements, such as lead and iodine in the perovskite compositions, relativistic effects play an essential role in their electronic structure. The band gap narrowing caused by SOC correction was shown by Umari *et al.*^{22,23} Beyond this vertical shift, the SOC accompanied by an inversion asymmetry might give rise to a more sophisticated spin-splitting in a halide perovskite. In the following, to elucidate the splitting of the energy level for the two different slabs, with various thicknesses, the band structure calculations were done, taking SOC into account. As illustrated in Fig. 4 both the orbital contributions and the spin texture pattern can be different with regard to the type of termination and thickness of slabs, as we will see in next sections.

A glance at the two band structures reveals the different responses of CsI- and PbI_2 -terminated slabs to the $\mathcal{E} = 0.001$ a.u. As shown in Fig. 5, after applying the external field,

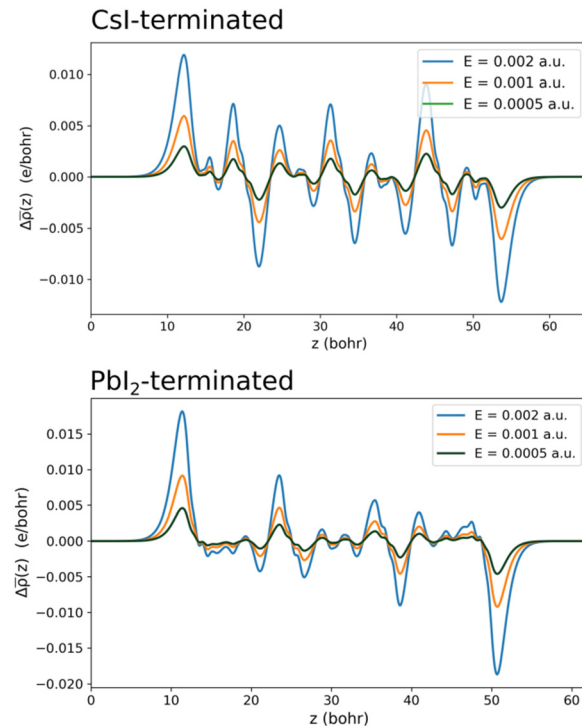


Fig. 3 The averaged induced charge densities generated by a range of external electric fields (0.0005–0.002 a.u.) along the z axis are shown for CsI-terminated (top), and PbI_2 -terminated (bottom) slabs.

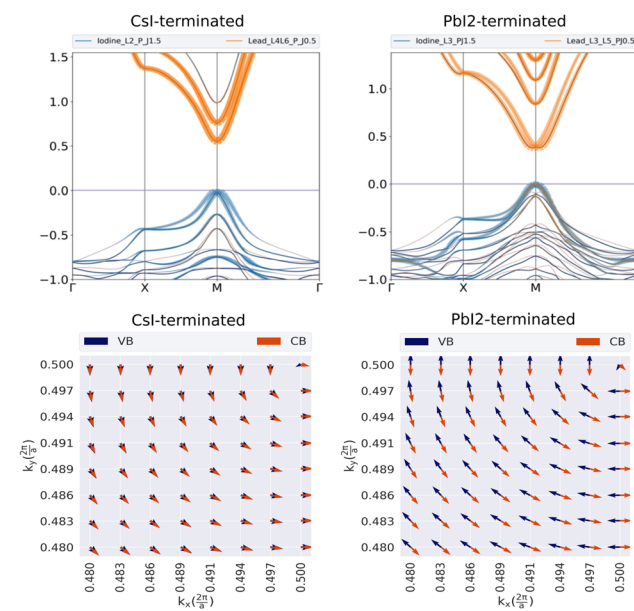


Fig. 4 The band structure of the CsI- and PbI_2 -terminated slabs for $n = 3$ (upper panel), and the corresponding spin textures (lower panel).

the band gap of the two slabs decreases at each thickness, with increasing electric field from $\mathcal{E} = 0.0005$ a.u. to $\mathcal{E} \simeq 0.004$ a.u., a dissimilar response to other electronic behaviors. The conduction and valence bands were split into two subbands. The spin for the two subbands is different: for CsI-terminated the

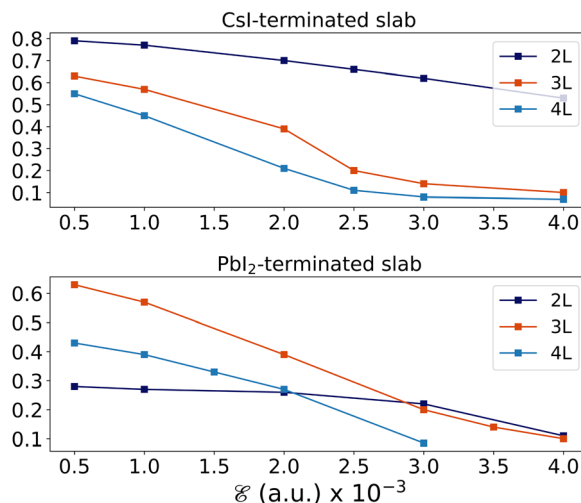


Fig. 5 The energy band-gap as a function of external field, for CsI- and PbI₂ terminated slabs with $n = 2, 3, 4$ thickness.

spin up and down are parallel, while the one for the PbI₂-terminated slab are in the opposite orientations, although for the subband of the neighbor bands, they can be parallel or antiparallel. From the excitonic transitions point of view, the spin orientation in the upper subband of VBM and the lower subband of CBM has a determining role in the electron–hole (e–h) recombination rate. While the parallel spin orientation in these two subbands facilitates the e–h recombination, their anti-parallel orientation might make a spin-forbidden transition.²⁴ Conducting a more in-depth analysis of the band splitting as a function of external field strength, the band separation along with Rashba parameters are calculated, and obtained for each slab as shown in Fig. 5.

As indicated in Fig. 6, for $n = 2$ the two types of termination show a semi-linear increase in the band splitting and Rashba parameters, however, this behavior is not consistent for the other thicknesses, $n = 3$ and $n = 4$. In these cases, maybe there is a turning point in the VBM or CBM, in which the Rashba parameters first decrease and then start to increase, or *vice versa*. As a result, the Rashba parameter must depend on the type of termination and thickness of slab. These results are in agreement with that of Yin *et al.* who showed that the Rashba splitting for the two types of termination of MAPbI₃ is strongly dependant on the number of atomic layers.²⁵ In addition, our results show that for the CsI-terminated slab at $\mathcal{E} = (0.0005 \text{ & } 0.001 \text{ a.u.})$, α_v almost converges for 2L, but for greater thicknesses, this behavior does not follow.

In cases where there is a turning point, for instance in CB bands from 3L of the PbI₂-terminated slab, raising the external electric field toward the point turning causes the gradual elimination of band splitting. Exploring the projection of valence band states over the atomic orbitals reveals that from the LCAO viewpoint, wave function corresponding to the valence band can be written as: $\psi_{v,k=M} = c_1\phi_1 + c_2\phi_2 + c_3\phi_3 + c_4\phi_4$ where ϕ_i is the iodine atomic p-orbital corresponding to the i -th layer.

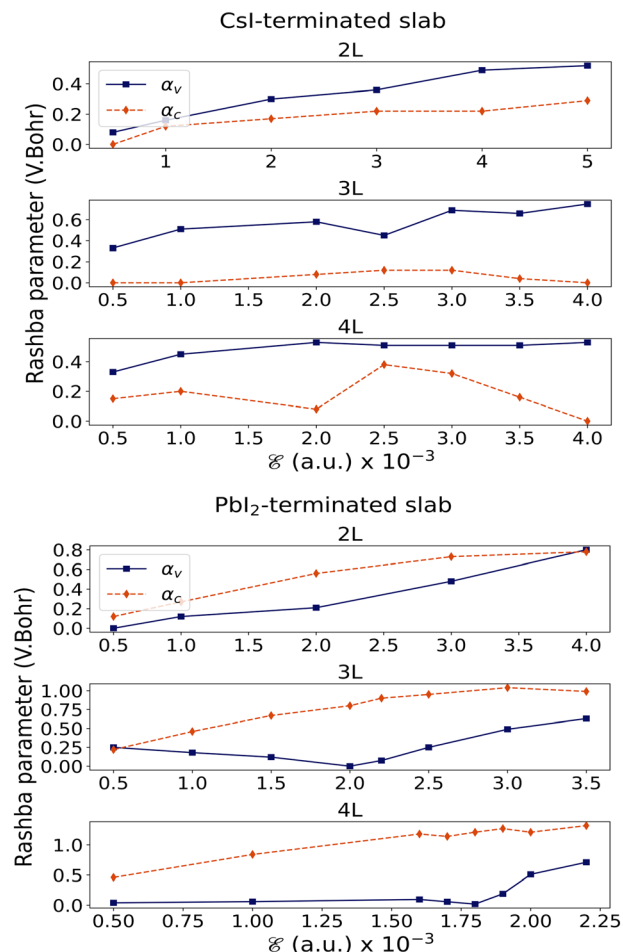


Fig. 6 Changes in Rashba parameters as a function of external field, for the valence and conduction bands in CsI- and PbI₂ terminated slabs with $n = 2, 3, 4$ thickness.

To gain more insight into these contributions, the isovalue surface of the $|\psi_n(r)|^2$ for the VBM and CBM wave functions at the extremum energies, are visualized in Fig. 7, the isosurface value is $\simeq 0.0011 \text{ \AA g}^{-3}$. As is clear from Fig. 7, at $\mathcal{E} = 0.0$ two interior PbI₂ layers provide the main contribution. Increasing the electric field in the z direction causes an effective potential gradient which shifts the atomic layers contribution in the VBM and CBM in the same direction. At a definite threshold field, this potential shift changes the order of the layers contribution to the valence band, and the outermost layer becomes the most dominant one. This gradual transfer of valence band wave function from interior to border layers, can explain the decline in the band splitting. Similar evidence for this effect is reported by Wang *et al.* for Ge quantum dots. According to these results there is a critical electric field whereby beyond this value, the Rashba parameter decreases.²⁶

Our results indicate that changes in the localization of the wave function quenches the splitting in larger fields and causes a significant drop in the Rashba parameter. To gain better insight into the environment effect, the planar averaged potentials, $\bar{V}(z)$, are calculated and visualized in Fig. 8. As is expected,

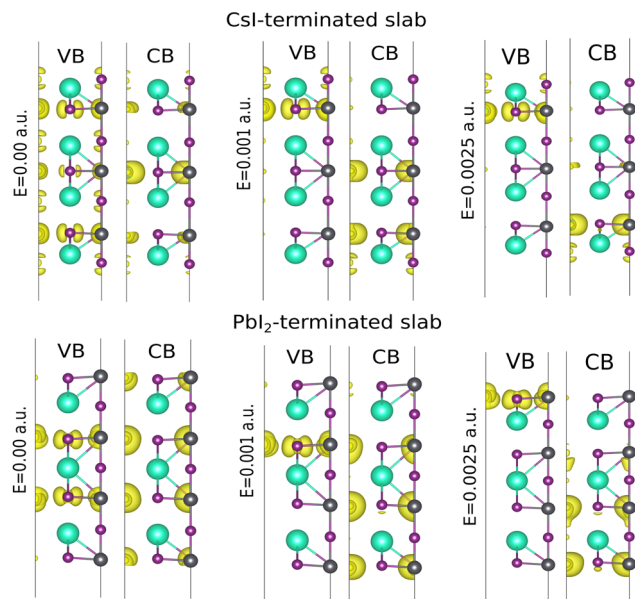


Fig. 7 Isosurface density of the valence and conduction edge wave function for $\mathcal{E} = (0.0, 0.001, 0.0025)$ a.u. Pb, I and Cs atoms are represented by the dark gray, purple and phosphor green, respectively.

increasing the external field leads to an effective shift in the extremum points of $\tilde{V}(z)$.

It should be noted that the VBM wave function can be described as a linear combination of four atomic orbitals, spatially localized on the potential wells corresponding to the PbI_2 layers. The relative displacement of these potential wells changes the contribution of the different layers in the VBM wave function and the energetically uppermost well has the dominant contribution. Application of the external field up to 0.001 a.u. shifts the well minima, however an inner layer still has the highest level of the potential minimum. Going from $\mathcal{E} = 0.001$ a.u. to 0.002 a.u., changes the potential wells in a way

whereby the outermost layer has the higher potential, and consequently the wave function shows more localization on the slab surface (see Fig. 7).

In summary, for a spatially fixed wave function, α_R changes linearly *versus* growth of the external field, analogous with the free electron gas. In contrast, if the electric field affects the spatial localization of the wave function significantly, changes in the potential gradient term ($\nabla\phi$) in the Rashba Hamiltonian became more complicated and the Rashba parameter does not follow a linear increase with the applied field.

3.4 Spin-texture

The relative orientation of the spin vectors corresponding to the conduction and valence bands are determining factors in electron–hole recombination time. To visualize the spin texture for CBM/VBM, the expectation values of the spin were calculated in the close neighborhood of extremum points of CBM/VBM bands. In this regard, for all given Kohn–Sham wave functions, $S_{iz,\vec{k}} = \langle \chi_{i,\vec{k}} | \sigma_z | \chi_{i,\vec{k}} \rangle$ are calculated, where σ_z ($z = 1, 2, 3$) are the Pauli matrix components, and $\chi_{i,\vec{k}}$ is i -th spinor eigen-function. The reciprocal lattice was sampled with M -centered 8×8 mesh, and \vec{k} stands for the wave-vector corresponding to each point. The spin texture of the two types of termination for different thickness n is calculated in a definite range of electric field and obtained patterns, depicted in Fig. 9–11.

As shown, the spin texture can be controlled with an external electric field, although the response of the two types of terminated slabs in various field ranges is not the same. For each slab, a lack of inversion symmetry and asymmetry charge distribution gives rise to a negative surface dipole or an internal electric field that can compensate by applying an external electric field. However, there are some points worth mentioning: first, as shown, in general, each type of termination has three spin patterns, in which spin up and down can be parallel in the clockwise or anti-clockwise, and/or be in anti-parallel directions. Nevertheless, there is an exception to this rule, the CsI-terminated slab for $n = 4$, has a single spin pattern throughout the range of the electric field, the anti-clockwise direction. In other cases, however, generally, there is a critical value of the external electric field beyond which leads to rotating the CBM or VBM spin vectors toward the other in the same direction or one of them travels in the opposite direction. For instance, the CsI-terminated slab with thickness $n = 3$, when the surface is exposed to the electric field, the pattern remains unchanged almost up to $\mathcal{E} \simeq 1 \times 10^{-7}$ a.u. (equivalent to 5.14×10^{-1} kV cm^{-1}), but increases with further electric field increase up to $\mathcal{E} \simeq 2 \times 10^{-7}$ a.u. (equivalent to 1.028 kV cm^{-1}); this pattern remains unchanged almost up to $\mathcal{E} \simeq 5 \times 10^{-7}$ a.u. (equivalent to 2.57 kV cm^{-1}), however, beyond this, the electric field leads to rotation of the CBM vector toward the VBM vector. This pattern maintains up to the higher fields, in this work almost up to $\mathcal{E} \simeq 4 \times 10^{-3}$ a.u. (equivalent to $2.056 \times 10^{+4}$ kV cm^{-1}) has been tested. A similar argument holds for the other slabs.

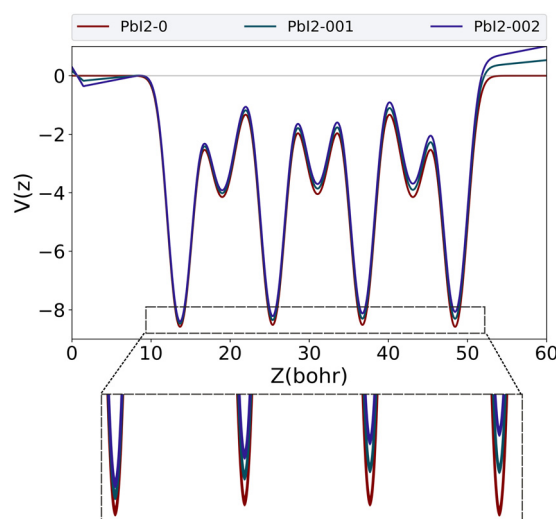


Fig. 8 Planar average of potential in the xy plane for the external fields: 0.0, 0.001, and 0.002 atomic unit.

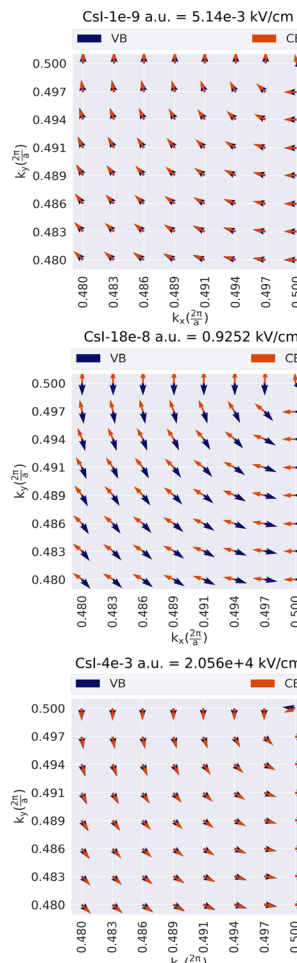


Fig. 9 Spin textures of spin vectors $S_{iz,k} = \langle \chi_{i,k} | \sigma_z | \chi_{i,k} \rangle$ are calculated, where σ_z ($\alpha = 1, 2, 3$) are the Pauli matrix components, and $\chi_{i,k}$ is the i -th spinor eigen-function in the k_x - k_y plane for CsI (left)- and PbI₂ (right) terminated with thickness $n = 2$ in weak and strong external fields.

As discussed above, in various ranges of the electric fields, the surface structures have different spin textures. It means that for the two types of termination, the electric field can act as a tuning parameter for the recombination rate of the charge carriers. For instance, there are ranges of the electric field that causes parallel orientation of the VBM and CBM spin vectors, which in turn leads to spin-allowed transitions. In contrast, the anti-parallel orientation of spin vectors gives rise to spin-forbidden transitions. Switching between the spin-allowed and forbidden states in the external field tuning is intriguing, in both optoelectronic and spintronic devices. Recently, it was established that all-inorganic perovskites under keV cm⁻¹ ($\sim 1 \times 10^{-7}$ a.u.) electric field show high piezoelectricity.²⁷ The obtained results in the present work indicate that such a small field can also be the determining factor in the spintronic properties of the system. Therefore the correlation between spintronic and piezoelectric parameters could be investigated in the future. Finally, the last point that should be considered is the influence of the presence of the turning points on the spin pattern. The results show that at the turning point for $n = 2, 3$

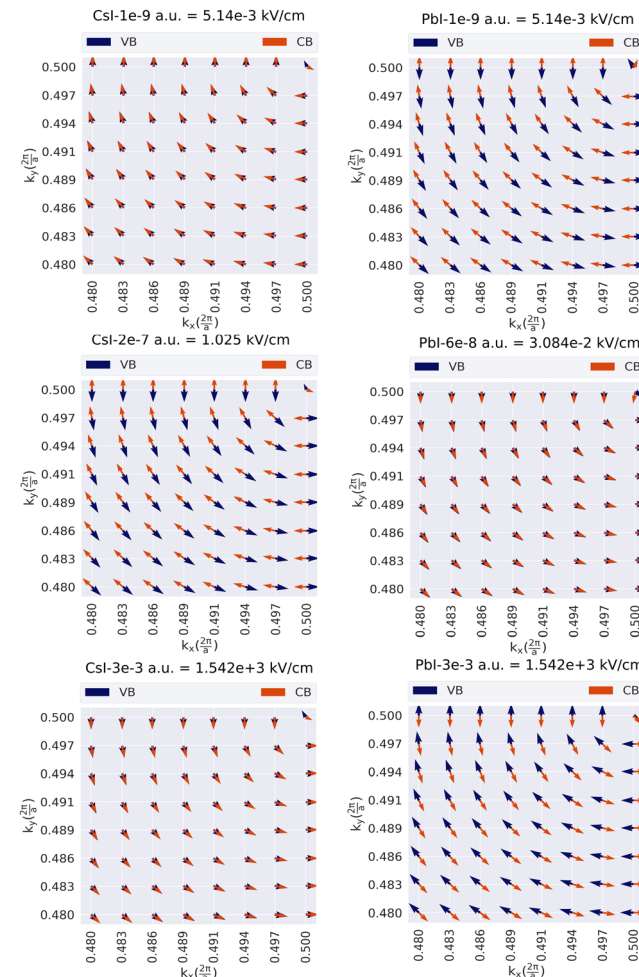


Fig. 10 Spin texture of spin vectors $S_{iz,k} = \langle \chi_{i,k} | \sigma_z | \chi_{i,k} \rangle$ are calculated, where σ_z ($\alpha = 1, 2, 3$) are the Pauli matrix components, and $\chi_{i,k}$ is the i -th spinor eigen-function in the k_x - k_y plane for CsI (left)- and PbI₂ (right) terminated with thickness $n = 3$ in weak and strong external fields.

(2L and 3L) the spin pattern maintains itself up to a high electric field. But this issue about the PbI₂ terminated slab for $n = 4$ (4L) is completely different. As shown in Fig. 12, the turning point plays a main role, and the VBM spin vector starts to rotate until they are in opposite directions to each other.

4 Summary and outlook

The present study was designed to determine the electronic structure for the two types of termination of the CsPbI₃ perovskite slabs in the presence of external fields. This study identified a tight correlation between the environmental variables and the SOC-induced band splitting of the CBM/VBM. In this regard, the electric field can be employed to tune the Rashba parameters and the spin texture for these systems. This can raise two distinct electron-hole recombination rates and spintronic responses for these two different terminations, which is determining factor for their optoelectronic applications. The non-linear behavior of the Rashba coefficient versus

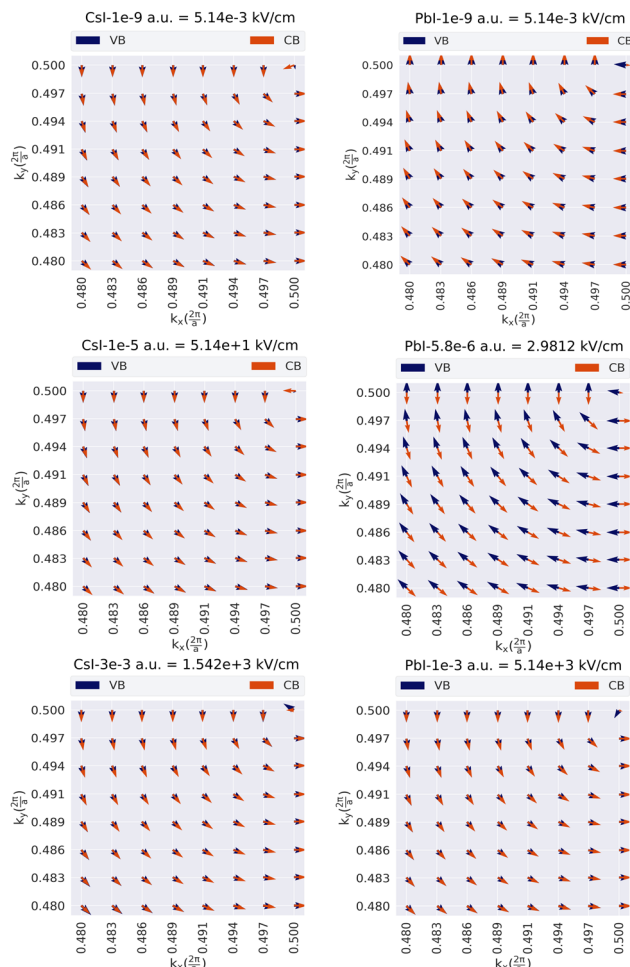


Fig. 11 Spin texture of spin vectors $S_{iz,k} = \langle \chi_{i,k} | \sigma_z | \chi_{i,k} \rangle$ are calculated, where σ_z ($\alpha = 1, 2, 3$) are the Pauli matrix components, and $\chi_{i,k}$ is the i -th spinor eigen-function in the k_x - k_y plane for Csl (left) and Pbl₂ (right) terminated with thickness $n = 4$ in weak and strong external fields.

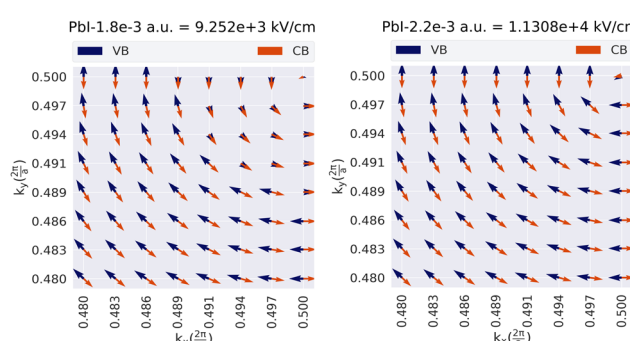


Fig. 12 Spin texture of spin vectors $S_{iz,k} = \langle \chi_{i,k} | \sigma_z | \chi_{i,k} \rangle$ are calculated, where σ_z ($\alpha = 1, 2, 3$) are the Pauli matrix components, and $\chi_{i,k}$ is the i -th spinor eigen-function in the k_x - k_y plane for the Pbl₂ terminated with thickness $n = 4$ around the turning point and higher values.

the electric field is concluded and explained in terms of changes in spatial localization of the wave functions corresponding to the CBM and VBM. The present findings confirm

the critical rule of built-in or external fields in tuning the spintronic properties of perovskite slabs. In summary, the band splitting quenching due to the change in the localization of wave function and the change of the spin texture behavior going from weak to strong fields, were two aspects not considered enough until the current work. The insights gained from this study may assist in tuning band splitting and designing spintronic related devices based on perovskite materials.

Conflicts of interest

There are no conflicts to declare.

References

- 1 G. Grancini and M. K. Nazeeruddin, *Nat. Rev. Mater.*, 2019, **4**, 4–22.
- 2 P. Schulz, D. Cahen and A. Kahn, *Chem. Rev.*, 2019, **119**, 3349–3417.
- 3 C. R. Kagan, D. B. Mitzi and C. D. Dimitrakopoulos, *Science*, 1999, **286**, 945–947.
- 4 G. Lin, Y. Lin, R. Cui, H. Huang, X. Guo, C. Li, J. Dong, X. Guo and B. Sun, *J. Mater. Chem. C*, 2015, **3**, 10793–10798.
- 5 K. Liao, X. Hu, Y. Cheng, Z. Yu, Y. Xue, Y. Chen and Q. Gong, *Adv. Opt. Mater.*, 2019, **7**, 1900350.
- 6 E. I. Rashba, *Soviet Phys., Solid State*, 1960, **2**, 1109–1122.
- 7 L. Leppert, S. E. Reyes-Lillo and J. B. Neaton, *J. Phys. Chem. Lett.*, 2016, **7**, 3683–3689.
- 8 J. Even, L. Pedesseau, J.-M. Jancu and C. Katan, *J. Phys. Chem. Lett.*, 2013, **4**, 2999–3005.
- 9 J. Even, L. Pedesseau, J.-M. Jancu and C. Katan, *Phys. Status Solidi RRL*, 2014, **8**, 31–35.
- 10 X. Zhang, Q. Liu, J.-W. Luo, A. J. Freeman and A. Zunger, *Nat. Phys.*, 2014, **10**, 387–393.
- 11 K. Shanavas and S. Satpathy, *Phys. Rev. Lett.*, 2014, **112**, 086802.
- 12 C. W. Myung, S. Javaid, K. S. Kim and G. Lee, *ACS Energy Lett.*, 2018, **3**, 1294–1300.
- 13 X. Chen, L. Liu and D. Shen, *J. Phys.: Condens. Matter*, 2018, **30**, 265501.
- 14 J. Chen, K. Wu, W. Hu and J. Yang, *J. Phys. Chem. Lett.*, 2021, **12**, 1932–1939.
- 15 P. Giannozzi, S. Baroni, N. Bonini, M. Calandra, R. Car, C. Cavazzoni, D. Ceresoli, G. L. Chiarotti, M. Cococcioni, I. Dabo, A. Dal Corso, S. de Gironcoli, S. Fabris, G. Fratesi, R. Gebauer, U. Gerstmann, C. Gougaud, A. Kokalj, M. Lazzeri, L. Martin-Samos, N. Marzari, F. Mauri, R. Mazzarello, S. Paolini, A. Pasquarello, L. Paulatto, C. Sbraccia, S. Scandolo, G. Sclauzero, A. P. Seitsonen, A. Smogunov, P. Umari and R. M. Wentzcovitch, *J. Phys.: Condens. Matter*, 2009, **21**, 395502.
- 16 P. Giannozzi, O. Andreussi, T. Brumme, O. Bunau, M. B. Nardelli, M. Calandra, R. Car, C. Cavazzoni, D. Ceresoli, M. Cococcioni, N. Colonna, I. Carnimeo,

A. D. Corso, S. de Gironcoli, P. Delugas, R. A. DiStasio Jr, A. Ferretti, A. Floris, G. Fratesi, G. Fugallo, R. Gebauer, U. Gerstmann, F. Giustino, T. Gorni, J. Jia, M. Kawamura, H.-Y. Ko, A. Kokalj, E. Küçük-benli, M. Lazzeri, M. Marsili, N. Marzari, F. Mauri, N. L. Nguyen, H.-V. Nguyen, A. O. de-la Roza, L. Paulatto, S. Poncé, D. Rocca, R. Sabatini, B. Santra, M. Schlipf, A. P. Seitsonen, A. Smogunov, I. Timrov, T. Thonhauser, P. Umari, N. Vast, X. Wu and S. Baroni, *J. Phys.: Condens. Matter*, 2017, **29**, 465901.

17 J. P. Perdew and A. Zunger, *Phys. Rev. B: Condens. Matter Mater. Phys.*, 1981, **23**, 5048.

18 J. M. Soler, E. Artacho, J. D. Gale, A. Garcia, J. Junquera, P. Ordejon and D. Sanchez-Portal, *J. Phys.: Condens. Matter*, 2002, **14**, 2745.

19 A. Garcia, N. Papior, A. Akhtar, E. Artacho, V. Blum, E. Bosoni, P. Brandimarte, M. Brandbyge, J. I. Cerdá and F. Corsetti, *et al.*, *J. Chem. Phys.*, 2020, **152**, 204108.

20 R. Cuadrado, M. Pruneda, A. Garca and P. Ordejón, *JPhys.: Mater.*, 2018, **1**, 015010.

21 T. Oguchi and T. Shishidou, *J. Phys.: Condens. Matter*, 2009, **21**, 092001.

22 P. Umari, E. Mosconi and F. De Angelis, *Sci. Rep.*, 2014, **4**, 4467.

23 D. Ji, M. Na, S. Wang, H. Zhang, K. Zhu, C. Zhang and X. Li, *Sci. Rep.*, 2018, **8**, 1–12.

24 F. Zheng, L. Z. Tan, S. Liu and A. M. Rappe, *Nano Lett.*, 2015, **15**, 7794–7800.

25 J. Yin, P. Maity, L. Xu, A. M. El-Zohry, H. Li, O. M. Bakr, J.-L. Brédas and O. F. Mohammed, *Chem. Mater.*, 2018, **30**, 8538–8545.

26 Z. Wang, *et al.*, Suppressing charge-noise sensitivity in high-speed Ge hole spin-orbit qubits, *arXiv*, 2019, preprint, arXiv:1911.11143, DOI: [10.48550/arXiv:1911.11143](https://doi.org/10.48550/arXiv:1911.11143).

27 D. B. Kim, K. H. Park and Y. S. Cho, *Energy Environ. Sci.*, 2020, **13**, 2077–2086.